2018/04/9

Thermal and compositional variations in the mantle inferred from the impedance contrast at the 410-km and 660-km discontinuities

AUTHOR: YOUCHUAN WANG

ADVISOR: NICHOLAS SCHMERR AND QUANCHENG HUANG

GEOL 394

I. ABSTRACT

Seismic discontinuities in the upper mantle are well-known and useful. They provide constraints on the thermal and compositional dynamics of the Earth. The goal of this study is to evaluate impedance contrast at the 410-km and 660-km discontinuities to find the density, temperature, and shear modulus of the transition zone globally. The global impedance contrast are compared to the impedance contrast under subduction zones and mid-ocean ridges. Mineral physics modeling is conducted based on the impedance contrast data collected; temperature, mineral composition, and phase condition are inferred from the impedance contrast data collected.

Based on the theory of mantle convection, impedance contrast of subduction zone is expected to behave differently from the global average. This project studies whether the increase of basalt fraction within the mantle transition zone beneath subduction zones would lower the impedance contrast at 410-km and 660-km discontinuities compared to the global average, or that the mantle transition zone discontinuities beneath subduction zones have an impedance contrast no different from the global average. At mid-ocean ridges, no differences are expected in discontinuities and impedance contrast between the regional values and the global average at 410-km and 660-km. Mineral physics modeling is used to study the impedance contrast at these areas as well.

The project also quantify the discrepancy of basalt fraction between the geochemistry model and mineral physics model of the upper mantle transition zone. It suggests different mechanisms to reconcile the discrepancy and tries to make the alignment of these two models. The mechanisms are corrections for attenuation, geometric spreading, and stack-defocusing.

II. TABLE OF CONTENTS

Contents

III. INTRODUCTION

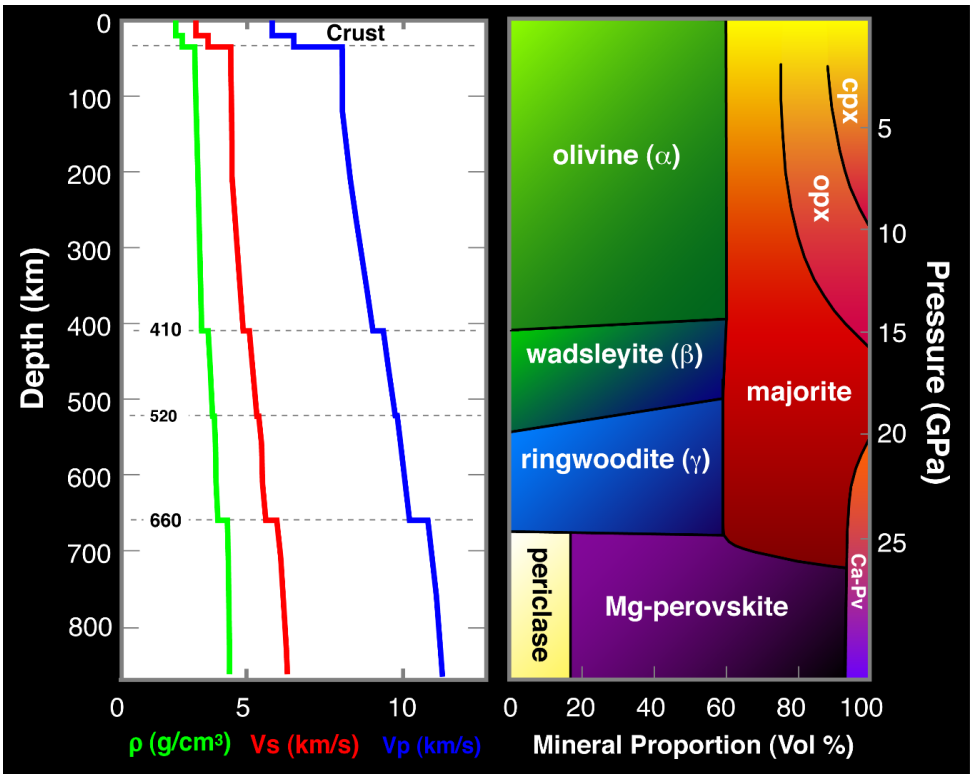

Figure 1. (Left plot) Illustration of discontinuity in the upper mantle, shear wave velocity and density versus depth. (Right plot) Illustration of the phase change of rocks at depth. Modified from Fei and Bertka, 1999.

The earth's mantle is divided into 3 parts, the upper mantle, the transition zone, and the lower mantle, as the result of sudden seismic velocity discontinuity at 410-km depth and 660-km depth. The transition zone is where the discontinuity happens, as shown in figure 1. On the left plot, Vs (shear wave velocity, red line) increases rapidly within few kilometers depth at 410-km, and-660 km (In this study 520-km discontinuity is not discussed). This sudden increase of seismic velocity, is defined as the discontinuity.

Based on previous knowledge of the Earth, at 410-km and 660-km depth [Shearer, 1999], rocks are experiencing phase changes due to increasing temperature and pressure, corresponding to the α-olivine to wadsleyite transition at the 400-km discontinuity, and ringwoodite to the Mg-perovskite + magnesiowüstite transition at the 670-km discontinuity [Ringwood, 1975], as the changes are showed in figure 1. These phase changes across a narrow interval at depth cause density contrast between top and bottom layer at 410-km and 660-km, and the velocity at which the seismic waves travel through each layer are affected. Because the phase change from α-olivine to wadsleyite is exothermic, 410-km discontinuity occurs at greater depth in a high temperature environment in the mantle, and because that from ringwoodite to Mg-perovskite + magnesiowüstite is endothermic, 660-km discontinuity occurs at shallower depth in a high-temperature mantle environment. The anti-correlated depth relationship between the 410- and

660- km discontinuity makes transition zone thickness an ideal thermometer for mantle [Schmerr and Garnero, 2006].

The observable in the project is amplitude of the seismic wave of both upper layer and bottom layer of the discontinuity. To get physical meaning such as depth and temperature from the property of seismic wave, impedance contrast is adopted. Impedance is the multiple of velocity of the seismic wave, the density of the material and the incident/reflected angle. The impedance contrast, is the ratio between the upper layer impedance to the lower layer impedance. The equation is as follows:

$$Z = \rho * V \quad \text{(Equation 1.)}$$

$$ImpedanceContrast = \frac{z2\cos\theta2 - z1\cos\theta1}{z2\cos\theta2 + z1\cos\theta1} \quad \text{(Equation 2.)}$$

To directly get values for density and velocity only, reflection coefficient is introduced. Reflection coefficient, is the impedance without the incident/reflection angle effect, or can be considered as 90 degree, then cos90 degree is 1. Reflection coefficient, can be calculated as amplitude of the reflected wave to the incident wave, or how much energy is reflected. The equation is as follows:

$$ReflectionCoefficient = \frac{z2 - z1}{z2 + z1} \quad \text{(Equation 3.)}$$

$$ReflectionCoefficient = \frac{A1}{A2} \quad \text{(Equation 4.)}$$

With reflection coefficient, physical properties of transition zone can be linked with the wave properties. Reflection amplitudes (reflection coefficient) vary due to impedance contrast in long-period observations [Chambers et al., 2005]. In this project, these properties of seismic discontinuities are studied: impedance contrast under the transition zones globally, and under small regional areas, including subduction zones and mid-ocean ridges. With the help of mineral physics modeling, information of physical properties at transition zone, i.e., temperature, mineral composition, and depth at which the discontinuities happen are inferred from the seismic wave observations at 440-km and 660- km discontinuities.

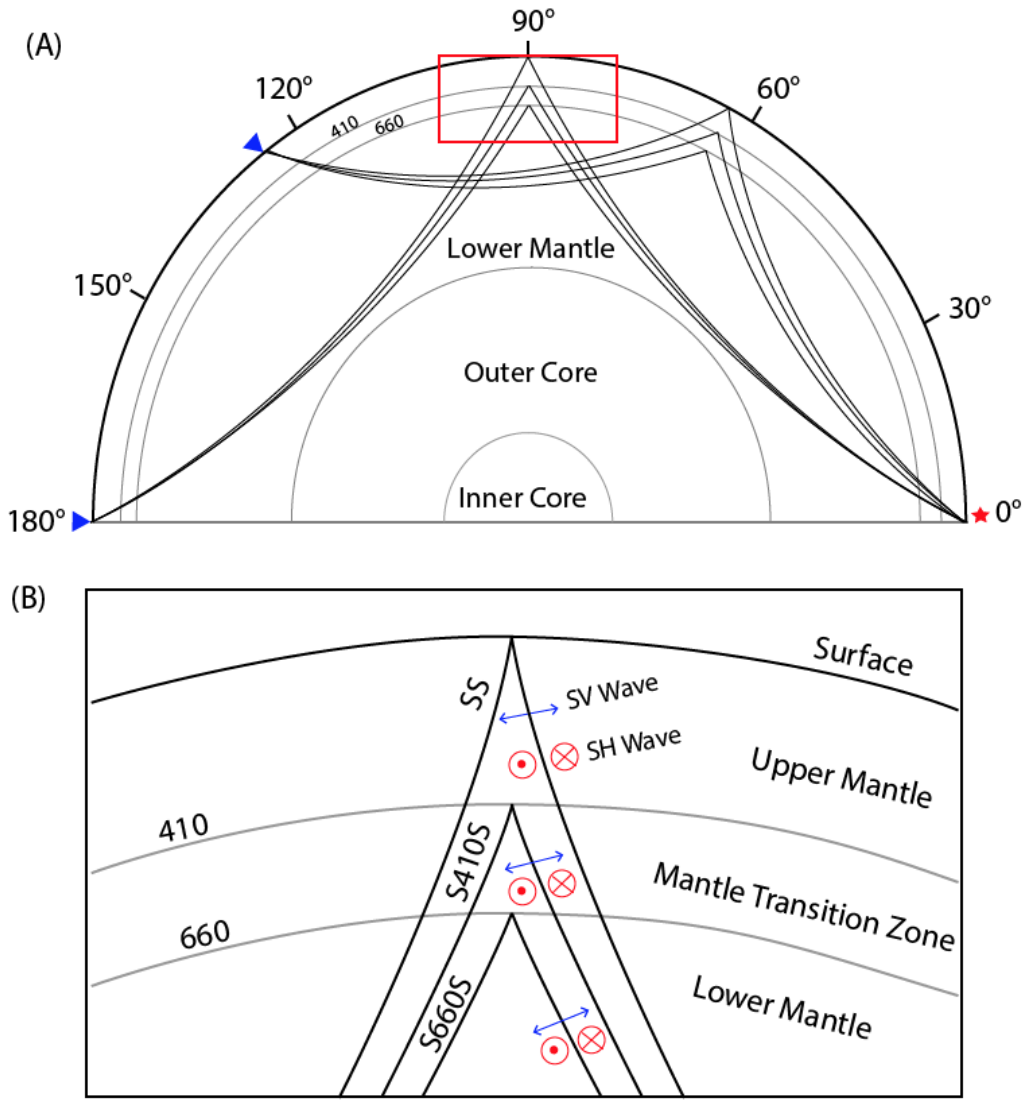

Figure 2. Schematic of an example data set displaying a seismic ray path of SS and its precursors. By Huang, 2017.

Long-period SS waves and its corresponding underside S410S and S660S precursor are used to determine large scale topography on a global scale [Flanagan and Shearer, 1999]. In this project, seismic data sets are analyzed from 100 degrees epicenter distance to 180 degrees epicenter distance globally of three different ray paths: SS, S410S, and S660S. To avoid/reduce the amplitude of incoherent noise and to increase the signal of the phases of interest, stacking method of seismic waves, which was broadly used by previous study (see Schmerr and Garnero, 2006; Bassin et al., 2000), is adopted in this project. The method is discussed with details in method of analysis section.

IV. OBJECTIVES

The study of regional differences between subduction zones/mid-ocean ridges and global

average can help test out the theory of mantle convection.

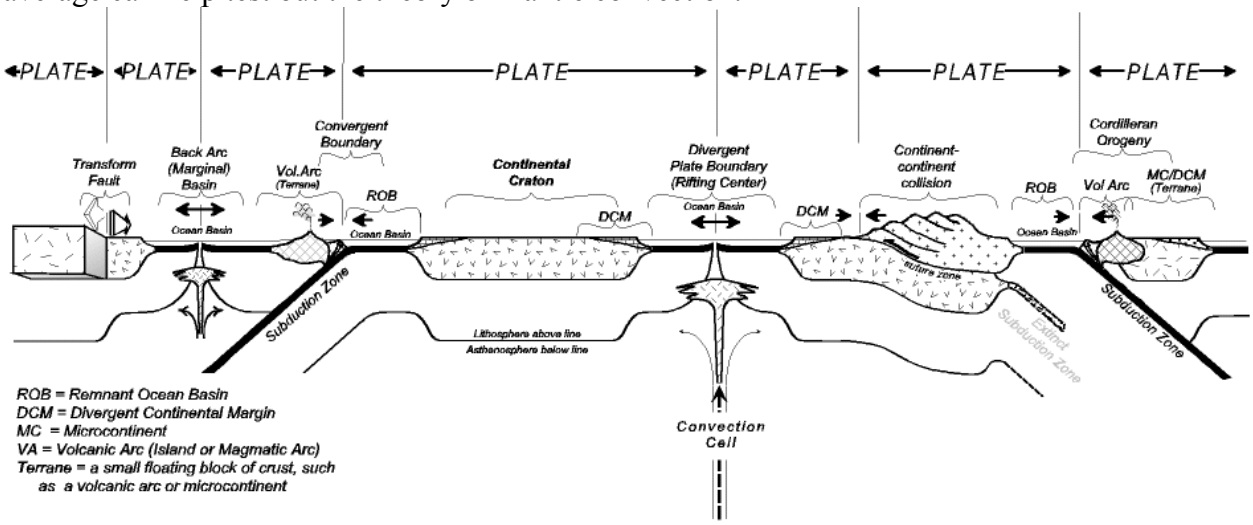

Figure 3. Illustrative picture of the theory of mantle convection of subduction zone and mid ocean ridge. Created by Fichter and Baedke, 2000.

There are two major structures discussed in the theory of mantle convection: mid ocean ridge and subduction zone. Because of the flow of heat within the Earth, certain areas at upper mantle are splitting due to the uprising heat, these structures are called mid ocean ridges. On the other hand, at the surface of the Earth, oceanic crusts are colder and then sink back into the Earth, these structures are called subduction zone. Graphical illustration of the theory of mantle convection is shown in figure 3. The mid ocean ridge is shallow structure, therefore there is no essential change of physical contacts at the transition zone. It is predicted that data collected from mid ocean ridge is the same as data collected globally. And as shown in the figure, under subduction zone, cold slabs from surface of the Earth are sinking into the transition zone, bringing materials of different mineral composition and temperature from those of transition zone. It is then predicted that data collected under these structures is different from global data.

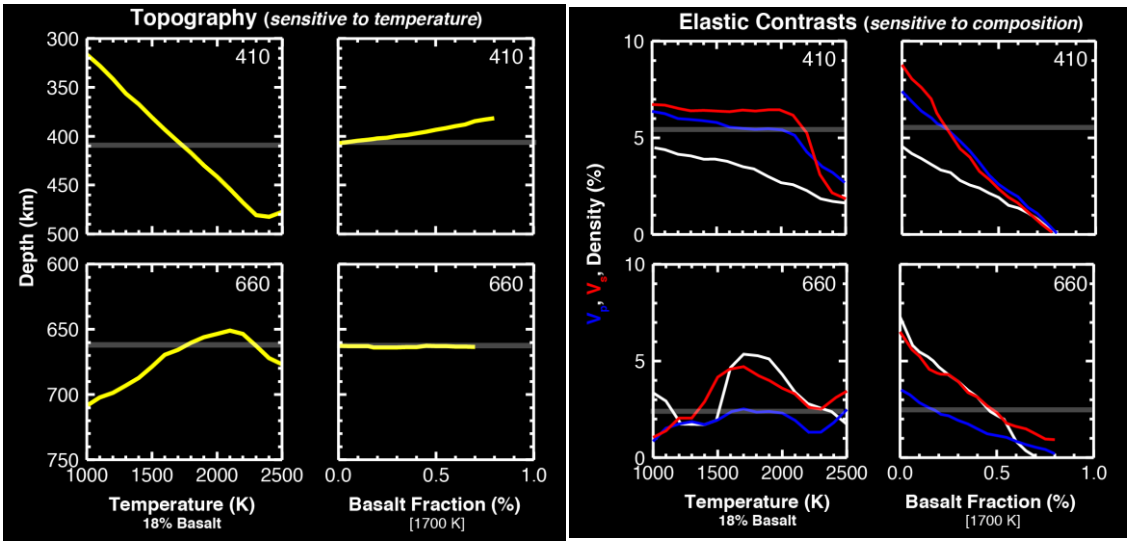

Figure 4. Topography (left) and impedance contrast (right) as a function of temperature and basalt fraction for both the 410 and 660; 4 collums of paried chart for 410 (top) and 660 (bottom). The first collum *is topography versus termperature when basalt fraction is fixed at 18%. The second collum is topography versus basalt fraction when temperature is fixed at 1700 K. The third collum is impedance contrast versus temperature when basalt fraction is fixed at 18%. Thr fourth collum is impedance contrast versus basalt fraction when temperature is fixed at 1700 K. By Xu et al., 2008.*

It is implied in the theory of mantle convection that under mid-ocean ridges, partial melting generates oceanic basalt crust and leaves behind its depleted residues, harzburgite. Under subduction zones, the denser ocean slab cools and then subducts into mantle with differentiated layers forming the slab: basalt and harzburgite [Ringwood, 1982]. Influences on the transition zone at subduction zone areas are discussed in Xu et al. (2008) and are showed in figure 4: transition zone topography, the depth at which 410 and 660 happen, is more sensitive to temperature; impedance contrast is more sensitive to bulk composition. When temperature is varied and basalt fraction is kept at 18%, as shown in the first column on the left, depth of 410-km discontinuity is decreasing as temperature decrease, and reaches 410-km depth at 1700 K; and 660-km discontinuity depth increases as temperature increases before 2000 K and decreases afterwards. When basalt fraction is varied and temperature is kept at 1700 K, as shown in the second plot, depth of 410 slightly increases as basalt fraction increase and depth of 660 isn't affected by basalt fraction at all. For impedance contrast, when temperature is varied and basalt fraction is kept at 18%, impedance contrast has complicated effect on 410 and 660. When basalt fraction is varied and temperature is kept at 1700 K, impedance contrast for both 410 and 660 decrease as temperature increases.

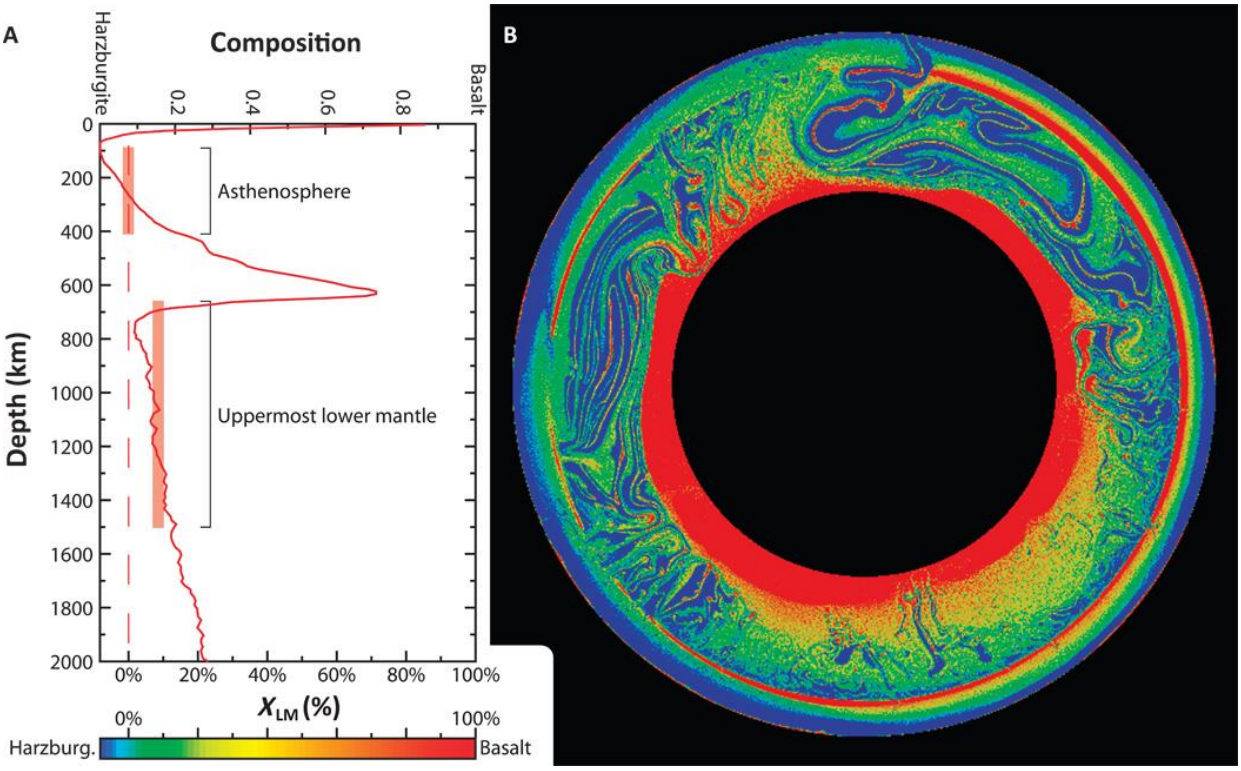

Figure 5. Average basalt fraction versus depth (left plot). Thermal convection simulation of mantle convection (right plot). From Ballmer et al, 2015.

In figure 5, the right plot shows the composition during the mantle convection process. The red color is basalt (relatively), the blue color is harzburgite, and the green and yellow colors are somewhere between these two materials. The plot shows basalt presents at CMB (core mantle boundary) and transition zone (as the peaks showed in the left plot). Large amount of harzburgite along with basalt come from the upper crust due to subduction, and goes back to the lower mantle, on the contrast, leaving behind the "depleted" basalt in transition zone. At mid-ocean ridges, due to viscosity contrast, shallow rock materials are concentrated, heated and used to make the crust, thus not affecting the material underneath, i.e., the transition zone. A good visualization of the mid ocean ridge structure is to think of layer of water on top of layer of honey, when someone uses straw to extract water from the surface of top, it doesn't uplift any honey from the bottom all the way up to the surface. And just like the straw doesn't uplift any honey, the spreading at the top of mid ocean ridge doesn't uplift any material from the core mantle boundary, therefore this structure doesn't affect the transition zone composition.

Because slabs consist of higher basalt fraction and has lower temperature subduct back into the mantle, corresponding hypothesizes are made.

Hypothesis I: An increase in basalt fraction within the mantle transition zone beneath subduction zones will lower the impedance contrast at 410- and 660- km discontinuities compared to the global average. Null: The mantle transition zone discontinuities beneath subduction zones have an impedance contrast no different from the global average.

Hypothesis II: Because oceanic ridges are expected to be shallow (<100 km) features, the impedance contrast of the mantle transition zone discontinuities under mid ocean ridges is similar to the global average.

V. METHODS OF ANALYSIS

1. Stacking Method and Discussion of Data Sets

As discussed in introduction, stacked data sets of SS, S410S, and S660S arrive from each epicenter consist of two additional pieces of information: amplitude and arrival time. These data are provided by Quancheng Huang, a graduate student of my advisor. I didn't gather the information myself but I did some research on how to gather the data. Firstly, the maximum amplitude of each SS wave of each epicenter distance is normalized so that the maximum amplitude is 1 and the arrival time is set to 0. Then use weighted stacks for each record according to its SS/SdS (S410S or S660S) signal-to-noise (SNR) ratio value for each epicenter distance. Each record is valued based on its level of noise in the SS domain and its level of interference in the precursor domain; if high level of noise or interference is determined, less weight is used when using this record to make the stack, and vice versa. Lastly, the precursor arrival time is stacked and measured correspondingly.

After the stacking methods, the SS maximum amplitudes are normalized to 1, and the corresponding arrival times are at 0. The precursor amplitudes (S410S and S660S) are calculated as ratios to the SS amplitude rather than actual amplitude (the value of corresponding amplitude is ~0.05). Their corresponding arrival times are negative because underside reflection precursors

arrive before waves in SS ray paths. Figure 2 shows one set of SS, S410S, and S660S data. For each epicenter distance, 2 precursors are normalized with respect to the SS wave.

There are three different data sets used in this project to test for the hypotheses. The first data set is for the global average. This data set collect seismic data of all structures worldwide. It has waves travel through continents, mid ocean ridges, subduction zones. This data set consists of the most data. From 100 degree to 180 degree with an interval of 0.5 degree. The software Slab 1.0 [Hayes et al., 2012] is used to analyze data in subduction zone model. It focuses subduction slabs around Pacific Ocean, and some areas in Indian Ocean. It has boundaries on Africa, North America, Japan, India, and Australia. The depths of slabs are from 0 to 300 km. This data set consists of the least data, from 100 degree to 180 degree with an interval of 4 degree. Mid-ocean ridges' locations and bounce points are determined by NUVEL-1 [DeMets et al., 1989]. It ranges from 100 degree to 180 degree with an interval of 2 degree. In this way, three different impedance contrast and reflection coefficient can be calculated from the observables focusing three different structures on the Earth. The result are compared to each other to study the similarity and difference.

2. Calculation of Impedance Contrast

A generic method is used in this project to acquire impedance contrast for global average, subduction zone and mid-ocean ridge. Firstly, find the maximum amplitude for each epicentral distance in the vicinity of the precursor 410 and 660 and its arrival time (+/-10 seconds are set to upper and lower bound). Plot amplitude and arrival time versus epicenter distance separately. Since all data are normalized according to the SS wave, the amplitude acquired here is the reflection coefficient. Then obtain error from the stacked data. The errors are 2 sigma, which is ~95% of the normal distribution coverage. After the systematic error bars are applied to the original reflection coefficient, geometric spreading and attenuation are taken into account, and corresponding corrections are made to them (detail discussions are in error discussion). Finally, reflection coefficient is converted to impedance contrast. This requires the incident/refracted angle and shear wave velocity, and these 2 variables are determined by TauP, which is a seismic travel time calculator. In addition to travel times, it can calculate derivative information such as ray paths through the earth, pierce and turning points by Crotwell et al., 1999.

The mathematical process is described by the following equation:

$$ReflectionCoefficient = \frac{Amp(SSPrecursor)}{Amp(SSWave)} \quad \text{(Equation 5.)}$$

$$ReflectionCoefficient = \frac{z2 - z1}{z2 + z1} \quad \text{(Equation 6.)}$$

TauP is used to determine the ray parameter (RP) for each reflection coefficient, then incident and refracted angle is determined from ray parameter by the following equation:

$$\sin(\theta 1) = \frac{RP}{v1}$$

$$\sin(\theta 2) = \frac{RP}{v2}$$ (Equation 7.)

Then impedance contrast can be induced from reflection coefficient with the incident and refracted angles:

$$ImpedanceContrast = \frac{z2\cos\theta 2 - z1\cos\theta 1}{z2\cos\theta 2 + z1\cos\theta 1}$$, where θ1 is incident angle and θ2 is the refracted angle. (Equation 8.)

3. Mineral Physics Modeling

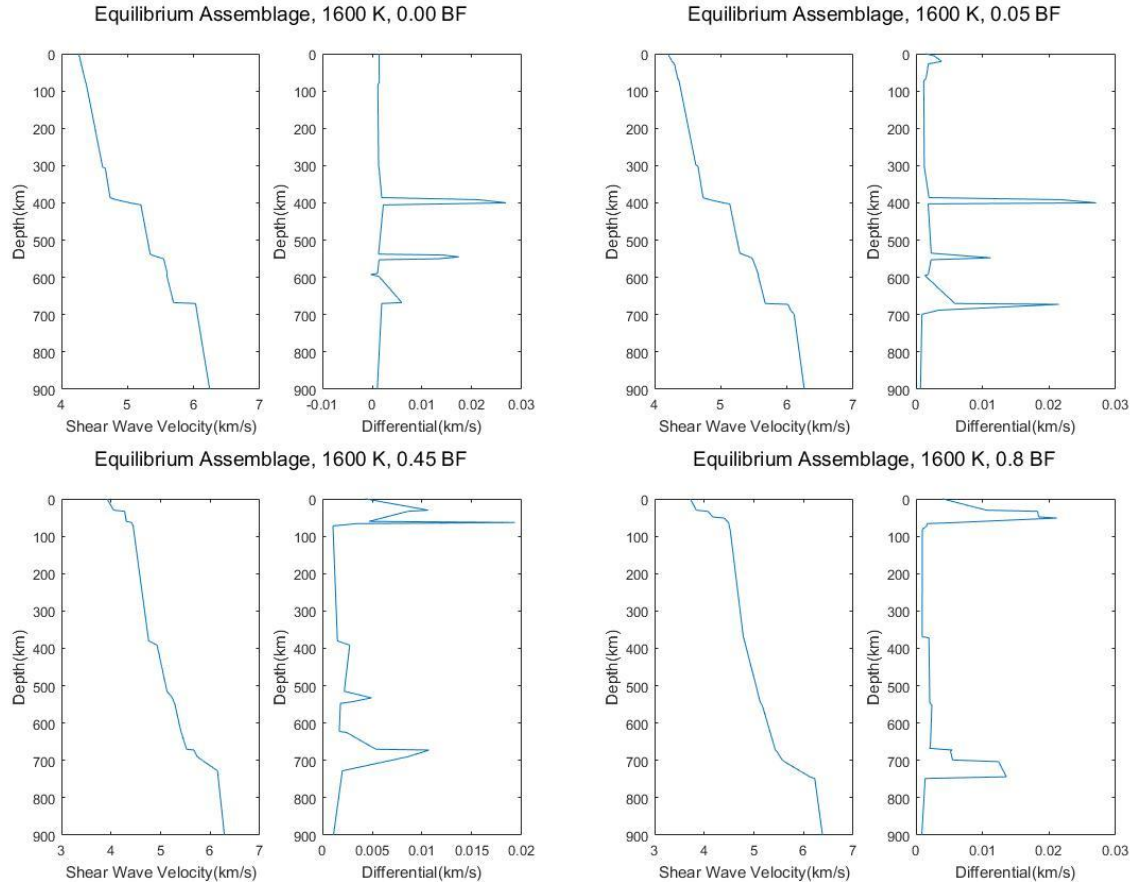

Figure 6. Examples of transition zone shear velocity versus depth.

Xu et al., (2008) database is used to construct a series of models of impedance contrast to test hypotheses for subduction zones and mid-ocean ridges against global average. The database ranges from 1000 K to 2500 K, with an interval of 100 K, and for each temperature, the composition range from 0% to 100% basalt fraction with an interval 5%. For each combination of temperature and composition condition, the database consists of shear wave velocity and density profile against depth. In total there are 672 independent combination of temperature and composition on the map of temperature and composition.

The discontinuity is determined manually under each temperature and composition condition. As shown in Figure 6, the 410-km and 660-km discontinuities are firstly determined by hands. Then corresponding density, velocity and depth are recorded to calculate for the impedance contrast. Boundaries of depth for 410-km discontinuity and 660-discontinuity are picked out based on the graph on the left; in some cases where the boundary is not clear, the differential of impedance contrast is used to pick out the boundary for 410-km and 660-km discontinuity. In figure 6, as basalt fraction goes up, the boundary for 660 becomes more obscure and the boundary for 410 diminishes. This is related to figure 1. If basalt fraction is 100%, then majorite takes over the whole composition chart. Shown in the right chart of figure 1, there would be no phase change at 410-km depth, therefore, there would be no discontinuity at 410-km depth. At 660-km depth, there would be a gradual phase change from majorite to perovskite. And this is shown by figure 6, as basalt fraction goes up, the boundary for 660-km discontinuity becomes obscure and gradual.

For all combinations of temperature and basalt fraction, the values of density and velocity are used to calculate for the impedance contrast for each 410-km discontinuity and 660-km discontinuity. Then every impedance contrast is compared by a least square misfit and a CHI^2 to every impedance contrast calculated previously for global average, mid ocean ridges, and subduction zone, with respect to corresponding degree range. For example, there will be a data set of density and shear velocity for the 410-km and 660-km discontinuity under condition of 1600 K and 0.05 basalt fraction. These values of density and Vs are used to calculate for impedance contrast. Then the impedance contrast is compared to ones calculated previously from the global average data set, mid ocean ridge data set, and the subduction zone data set. For global average, the impedance contrast is compared from 100 degrees to 180 degrees with an increase of 0.5 degree. For mid ocean ridge data set, the impedance contrast is compared from 100 degrees to 180 degrees with an increase of 2 degree. And for subduction zone, the range is from 100 degrees to 180 degrees with an increase of 4 degree. The least square misfit is that:

$$\sum_{degree}^{range} (IC(Xu'smodel) - IC(Observables))^2 / IC(Observables)^2 \qquad \text{(Equation 9.)}$$

The equation for CHI^2 used is as follows:

$$\chi^2 = \sum_{degree}^{range} (IC(Xu'smodel) - IC(Observables))^2 / Error(Observables)^2 \qquad \text{(Equation 10.)}$$

After calculation, for each method, 6 colored map are made to represent the results. The X axis is basalt fraction, the Y axis is temperature, and the color bar represents the misfit calculated. The 6 maps are impedance contrast from Xu's database for 410-km discontinuity, 660-km discontinuity compared to observables of global averages, mid ocean ridges, and subduction zone.

VI. PRESENTATION OF DATA, AND ANALYSIS OF UNCERTAINTY

1. Global data

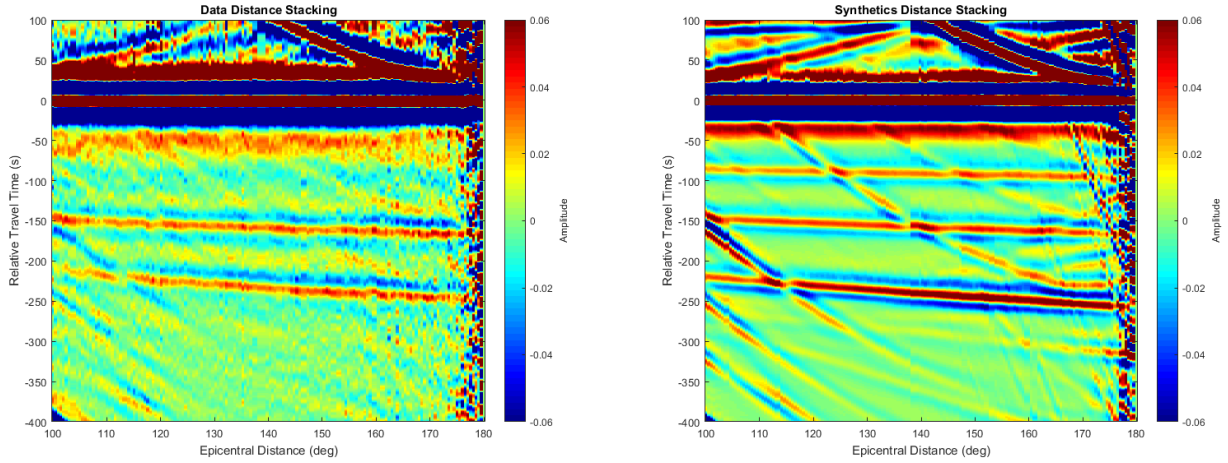

Figure 7. Observational (left) and synthetic (right) seismogram. It has three degrees of freedom; x axis epicenter distance; y axis arrival time; color stands for the amplitude of the wave at (x,y), from blue to red interpolated as -0.06 to 0.06.

The seismograph is a general representation of the seismic wave data. It includes comprehensive information. The X axis is epicenter distance; y axis is arrival time; color bar stands for the amplitude of the wave at (x,y), from blue to red interpolated as -0.06 to 0.06. Because everything is normalized with respect to SS wave, the red line at 0 arrival time is the SS wave, the red line at around -150 seconds arrival time is the S410S precursor, and at -200 seconds arrival time is the S660S precursor. Information about amplitude and arrival time versus depth can be separated from one seismograph and can be drawn as the following separate graph for clearer illustration in figure 8.

The observational seismogram (left) is based on actual data collected from stations all over the world, while the synthetic seismogram (right) is based on data calculated from mathematical models. Therefore, the observational is noisier and more scattered than the synthetic is due to experimental factors. In the project, observational is used and synthetic is put here for reference only.

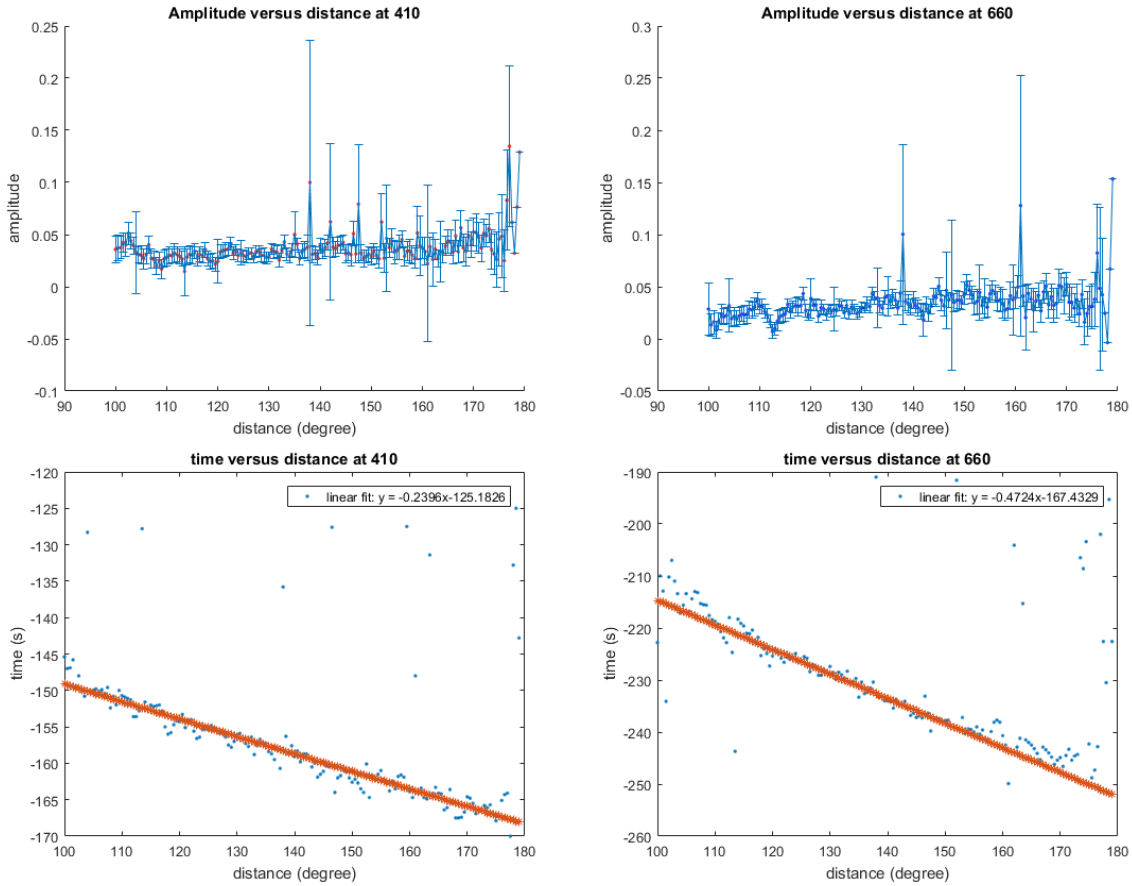

Figure 8. Schematic of data derived from the observational seismogram. . It has 160 data points from 100 degree to 179.5 degree with an increment of 0.5 degree. Amplitude of precursors at 410 and 660 (top) versus time. Arrival time of precursor at 410 and 660 (bottom), with lines linear fitted to the data ignoring the outliers. Red lines at the bottom graphs are estimation linear fit for the travel time scatter.

The characteristics existed in seismograph can be found in the separated amplitude profile: in figure 8, a valley exists between 102 degrees to 106 degrees on the plot of the 410 precursor amplitude, and a valley between 109 degrees to 116 degrees in the 660 precursor amplitude. In the original seismograph, between these intervals, there are other ray paths interfering with S410S and S660S, and this is reflected in the amplitude profile plots.

At some specific epicenter distances, e.g., 138 degrees of 410 precursor, the error bar is relatively big compared to others, but there are no geophysical features showed in seismogram at those specific locations. This is due to the lack of data. For most epicenter distance, there are abundant seismic profile to stack with, and the errors are small. At certain distance, e.g., 138 degree of the 410 precursor, there is little seismic profile to stack with, therefore the errors are large. Amplitudes with error bars that are in the negative quadrant are left out when doing the calculation, because amplitudes with error bars to the negative quadrant have the chance to be negative values, i.e. amplitudes that have changed polarities from the incident SS waves, and because amplitudes used in calculation need to be 100% sure in phase with the incident SS waves, otherwise negative values would generate undesired impedance contrast in wrong direction.

2. Reflection Coefficient (by PREM model)

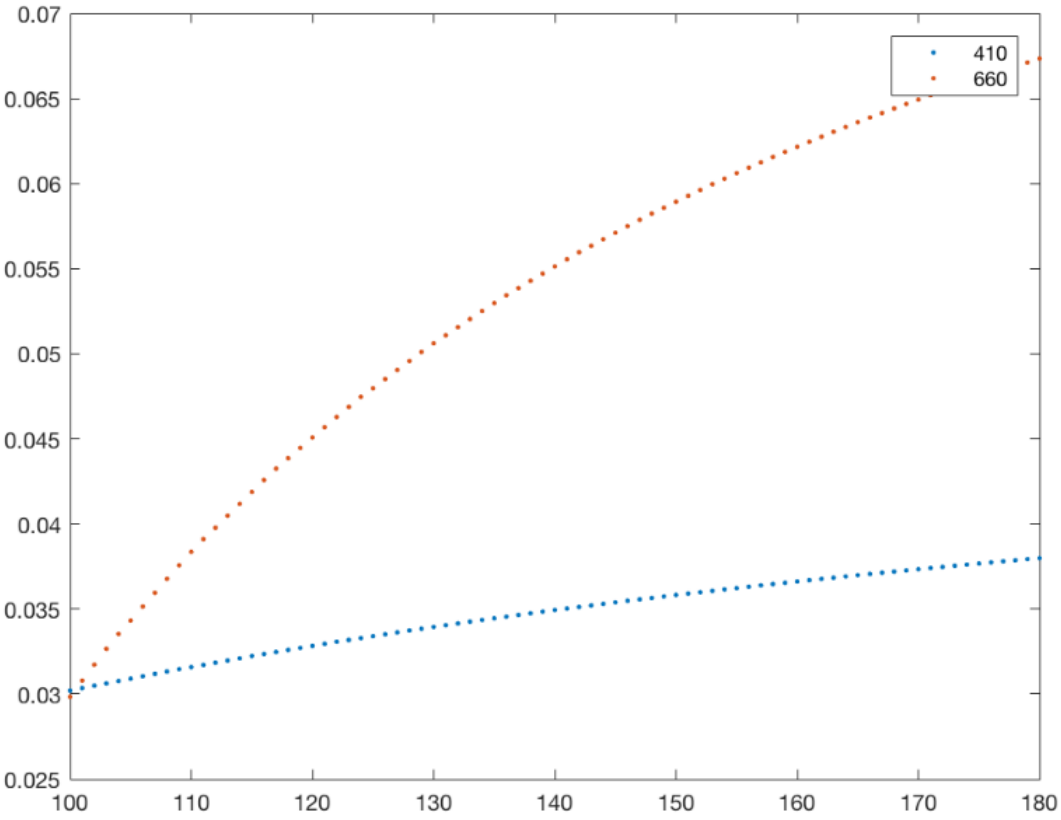

Figure 9. Reflection coefficient calculated by using the PREM model.

This impedance is calculated based solely on PREM model, using pure mathematics. Ray parameter is derived using TauP. Shear velocity and density of the earth are read off from PREM model.

3. Subduction zone

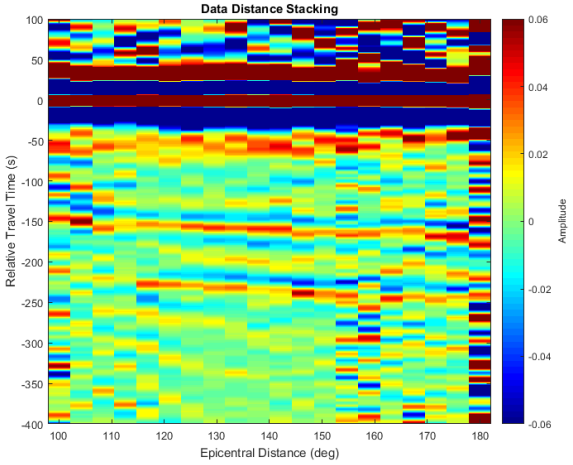

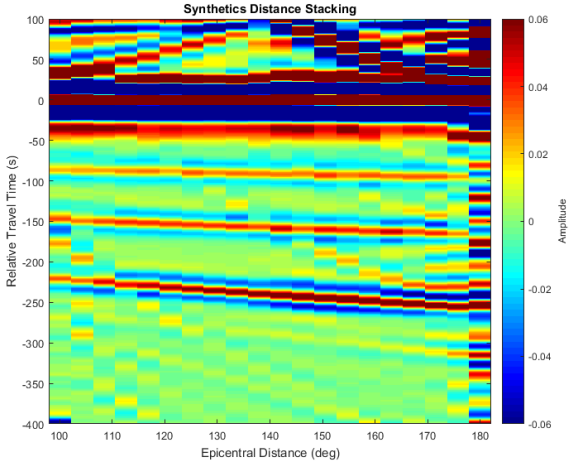

Figure 10. Seismogram of subduction zone data, with an interval of 4 degree in epicenter distance for each bin, from 100 degree to 180 degree. Observational (left) and synthetic (right).

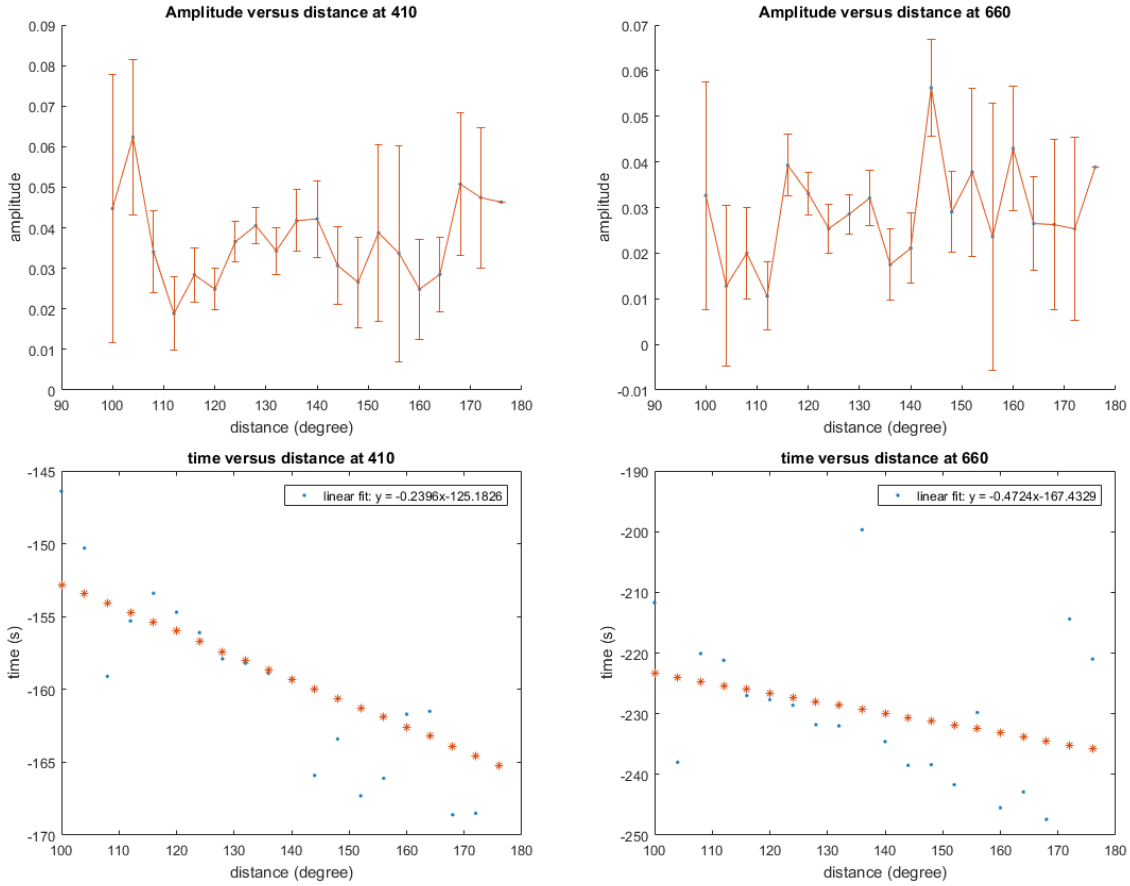

Figure 11. Plots of data retrieved from seismogram of subduction zone environment. It has 20 data points from 100 degree to 180 degree with an increment of 4 degree. Amplitude of precursors at 410 and 660 (top) versus time. Arrival time of precursor at 410 and 660 (bottom), with lines linear fitted to the data ignoring the outliers. Red lines at the bottom graphs are estimation linear fit for the travel time scatter.

4. Mid-ocean ridges

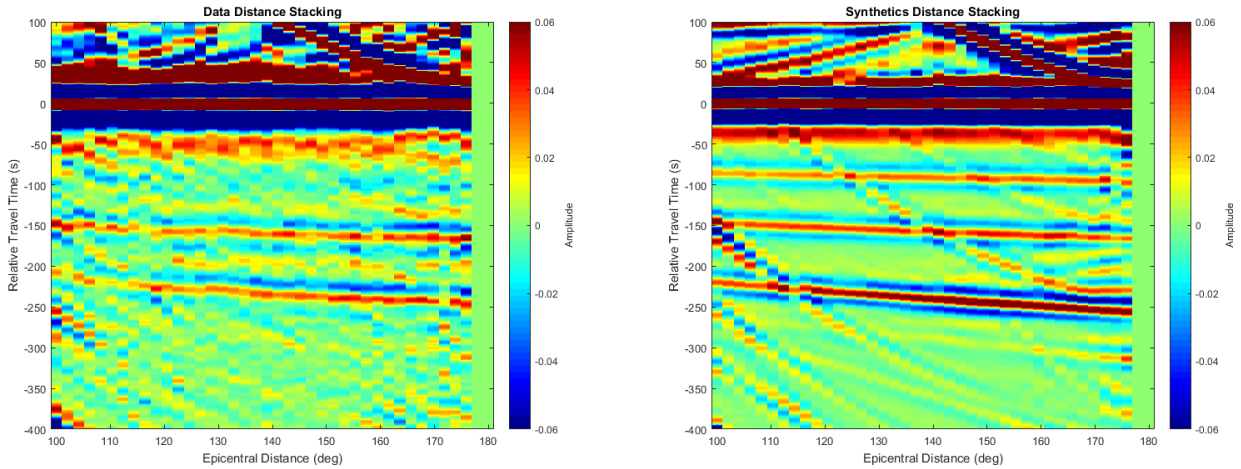

Figure 12. Seismogram of mid-ocean ridge data, with an interval of 2 degree in epicenter distance for each bin, from 100 degrees to 180 degrees. Observational (left) and synthetic (right).

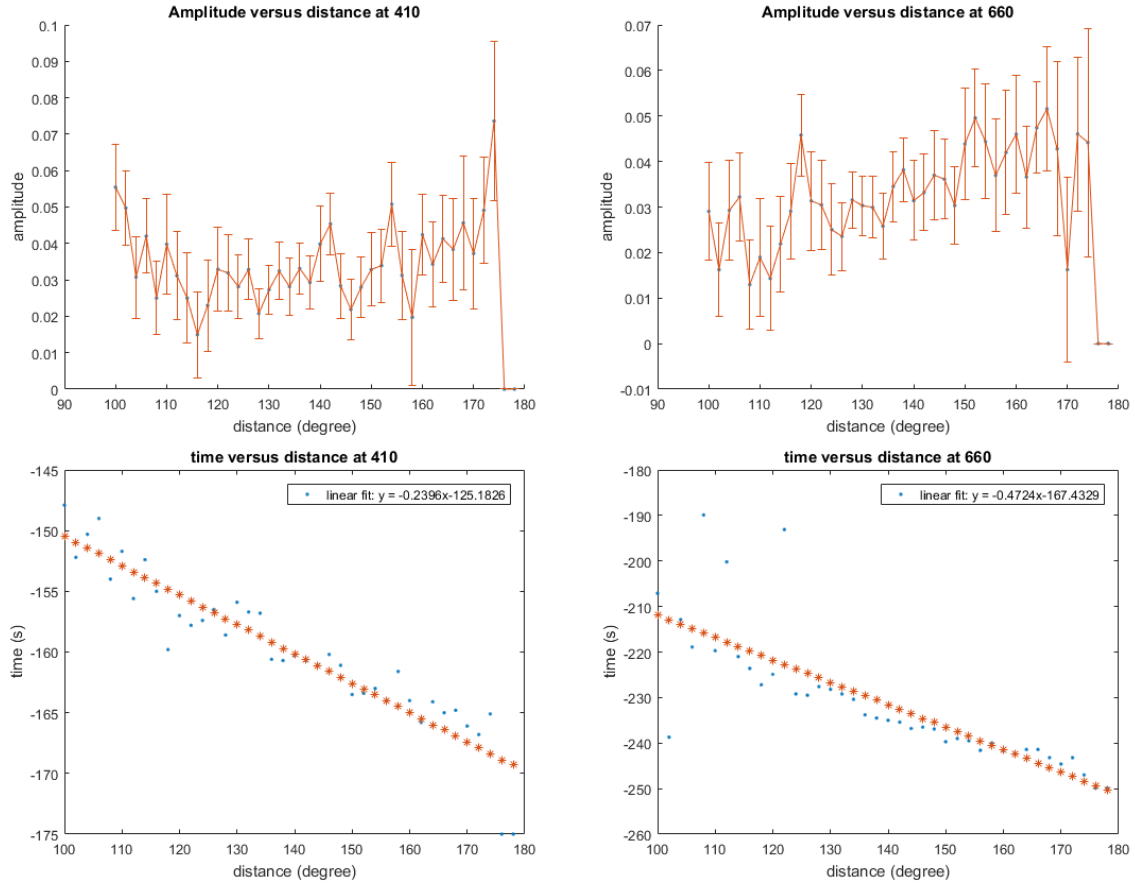

Figure 13. Plots of data retrieved from seismogram of subduction zone environment. There are 40 data points from 100 degree to 180 degree with an increment of 2 degree. Amplitude of precursors at 410 and 660 (top) versus time. Arrival time of precursor at 410 and 660 (bottom), with lines linear fitted to the data ignoring the outliers. Red lines at the bottom graphs are estimation linear fit for the travel time scatter.

There are 20 data points in the subduction zone environment and 40 data points in the mid-ocean ridge environment, because subduction zone environments are rarer in sparser than mid-ocean ridges'. Therefore, subduction zone data are concluded from a wider range of epicentral distance to ensure a better data quality. As discussed in the hypotheses, impedance contrast is expected to be different from global average in the subduction zone environment and is expected to be similar to the global average in the mid-ocean ridge environment. Thus, as it is showed in the data plots above (figure 11 and figure 13), there are differences in the reflection coefficients calculated. To test for the hypotheses, impedance contrast is then induced from these data sets using the methods discussed above. Then the regional impedance contrast is then compared against the global average. Three impedance contrasts are used to fit the mineral physics models. And then the final results are compared against each other to see whether they match the hypotheses.

5. Comparison of Impedance Contrast

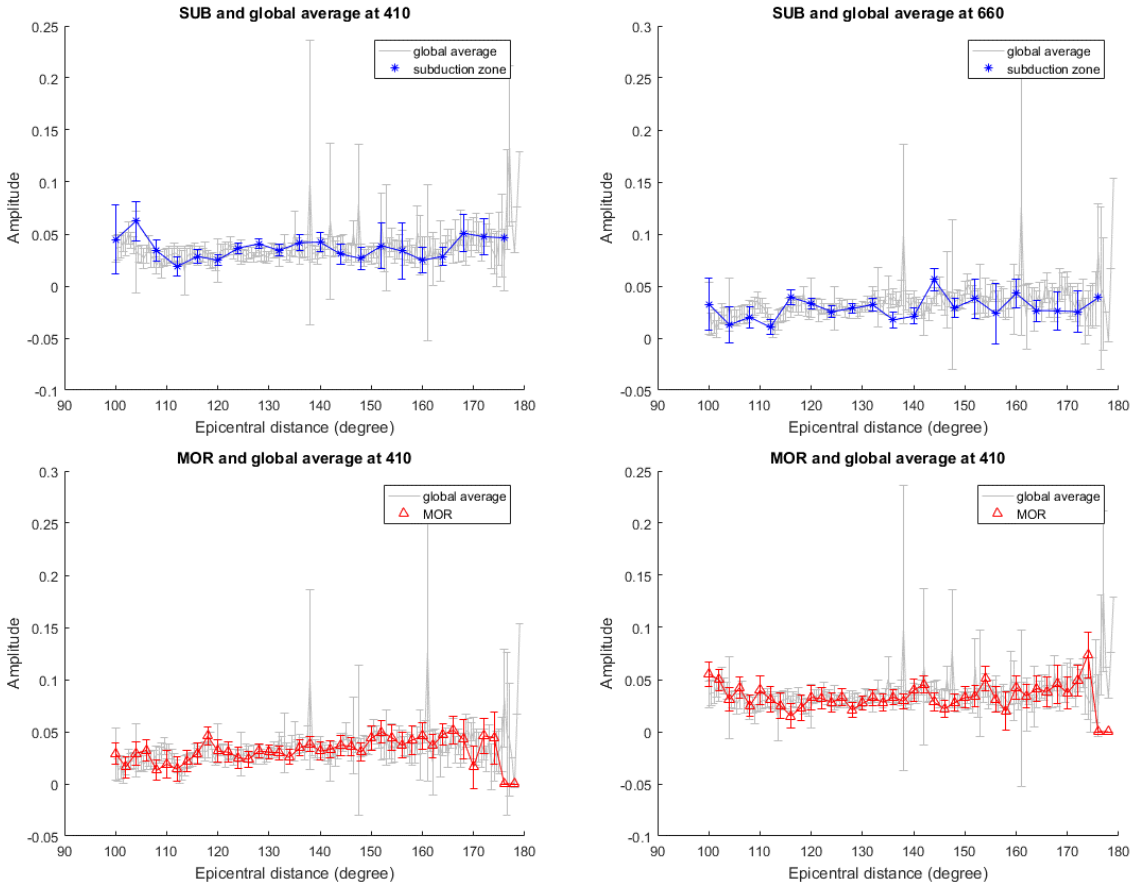

Figure 14. Impedance contrast of SUB (subduction zone) and MOR (mid ocean ridge) against that of global average.

Impedance contrast for both SUB and MOR are plotted, with global average (grey color) in the back ground using Matlab code. As shown in figure 14, it is hard to tell the accurate comparison between the variables: whether the impedance contrast is lower or higher; and no value for the

depth at which discontinuity happens. Impedance contrast need to be evaluated to the corresponding values for depth, density, and velocity in order to test the hypothesis.

6. Mineral Physics Modelling

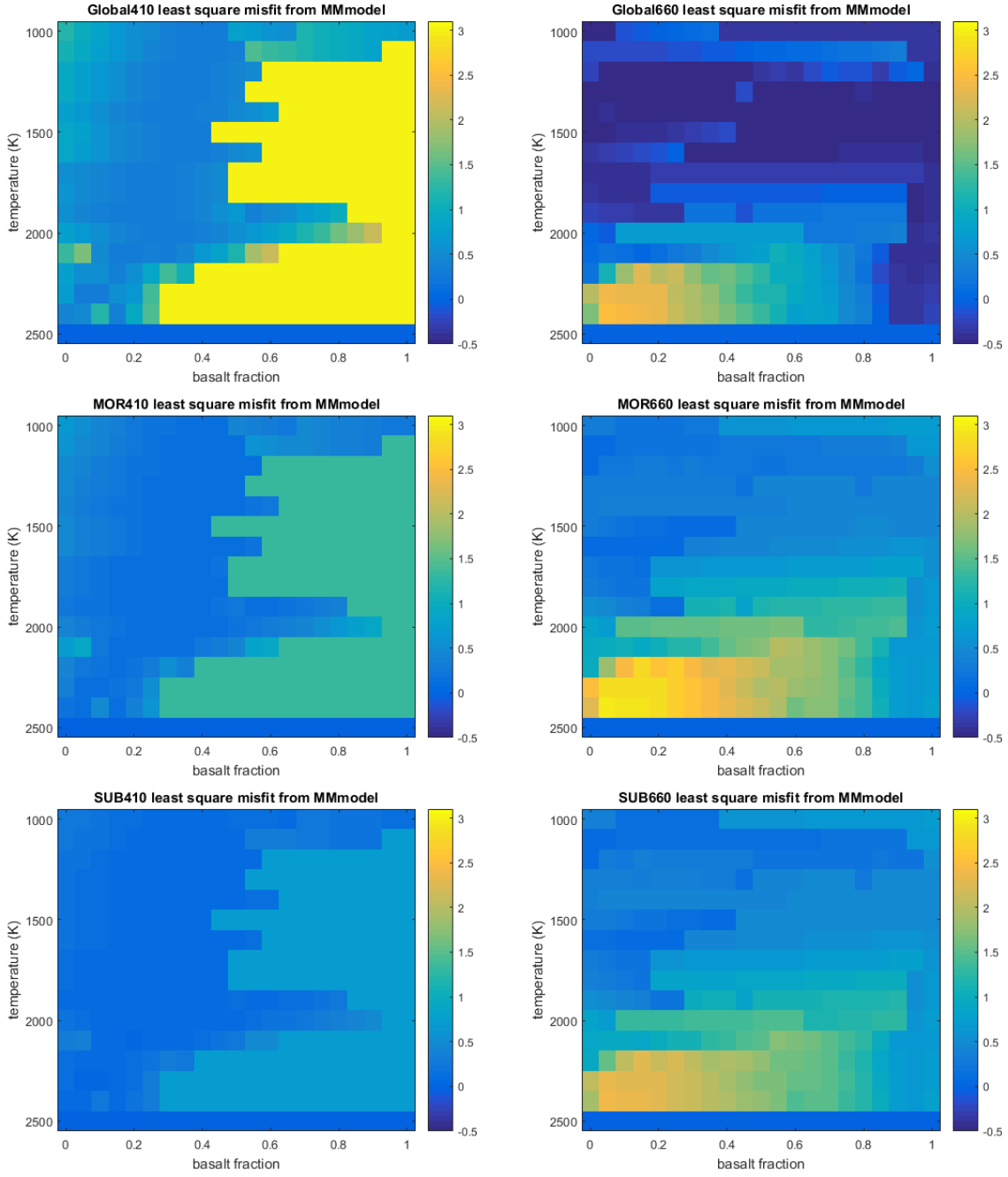

Figure 15. Color map of least square impedance contrast misfit of MMmodel (mechanical mixture model) in Xu's model from impedance contrast of SUB, MOR, and global average.

As discussed in the previous section, mechanical mixture model from Xu's model is used to calculate for the impedance contrast. The results are compared to the impedance contrast calculated using data collected under MOR, SUB and the global average. There are 6 colored

map; for each map, there are 16*21 = 726 data points standing for data from 1000 K to 2500 K with an interval of 100 K in temperature and 0.00 to 1.00 with an interval of 0.05 in basalt fraction. Each data point represents the summation of misfit of the impedance contrast of Xu' model from that of the observable data of each degree (MOR, SUB and global average) by using color bars.

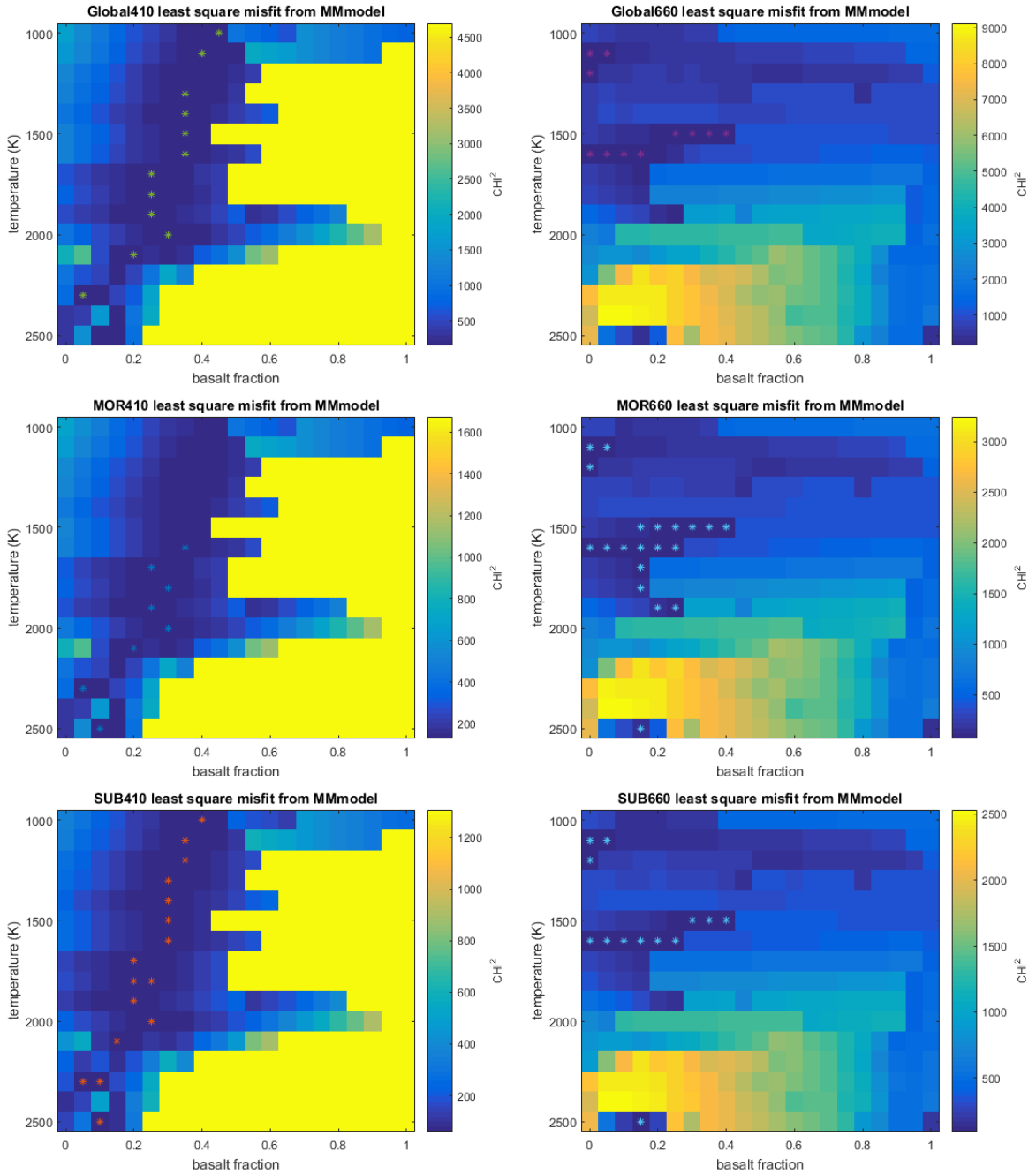

Figure 16. Colored CHI^2 MAP FOR MMmodel (mechanical mixture model) in Xu's model from impedance contrast of SUB, MOR, and global average. Data within 95% confidence interval are marked with stars.

CHI^2 method is adopted in the project to incorporate error bars in the observables. The equation is as follows:

$$\chi^2 = \sum_{degree}^{range} (IC(Xu'smodel) - IC(Observables))^2 / Error(Observables)^2 \quad \text{(Equation 11.)}$$

Then CHI^2 table is compared to find the 95% confidence interval.
The CHI^2 method is solid for most epicenter degrees, but there are epicenter degrees that are skipped using CHI^2 method, because the error bars of those degrees are so low, that every value of temperature and basalt fraction is indistinguishably large. Therefore, CHI^2 table and misfit table should be considered along with each other to give better comprehension.

7. Geochemistry modelling

Table 1. Bulk composition in mol% (Xu et al., 2008)

Component	Pyrolite	Basalt	Harzburgite	Modified harzburgite
SiO_2	38.71	51.75	36.07	36.04
MgO	49.85	14.94	56.51	56.54
FeO	6.17	7.06	6.07	5.97
CaO	2.94	13.88	0.81	0.79
Al_2O_3	2.22	10.19	0.53	0.65
Na_2O	0.11	2.18	0.00	0.00

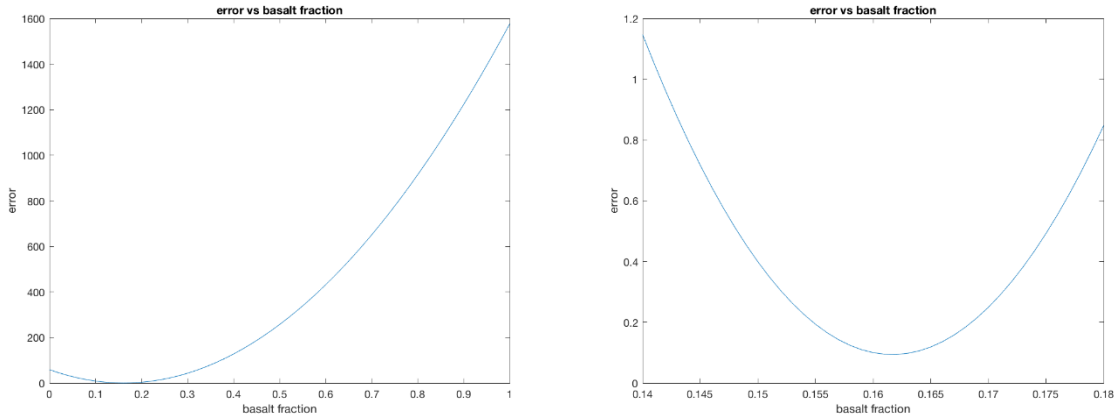

Figure 17. Geochemistry model of error versus basalt fraction in the upper mantle.

The table 1 by Xu et al. (2008) is used to calculate for the basalt composition in the bulk upper mantle. The upper mantle is divided into basalt and harzburgite, and the composition is used to determine what fraction of basalt and harzburgite is in the upper mantle to make pyrolite. The percentage of basalt that gives the least misfit of the chemical element is calculated. The value of basalt fraction determined for geochemistry model is **0.162**.

8. Discussion of Errors

a) Errors of amplitudes observed

Errors are given along with the original data set. For each epicenter distance, the data set gives both the amplitude and the error associated. Errors then are applied to the amplitudes in the graph, as shown in figure 9, 11, 13, etc. These error bars are 2 sigma range, which is ~95% of the normal distribution coverage. Seismic data are collected by using bootstrap method. This method is stable under large range of noise condition and can be used to distinguish between data with no splitting, data with splitting and noisy data [Sandovl and Hearn, 1994]. Bootstrap method works by selecting random sets of repeated seismic waves and normalizing the combination of them together as an individual data. Then normalize the combination of all data as the mean value. Finally calculate the variance by using the regular stand deviation formula. Because of the bootstrap method, there are unequal distribution of errors. At some epicenter distance, there are more seismic data collected and stacked, therefore the error associated with this epicenter distance is small. There are epicenter distances with little seismic data associated. At those distances, because few seismic data are stacked to generate the data, errors are large. As shown in figure 8, at 410-km discontinuity, at most epicenter distances, the error bars are short, about 0.025. At 138 epicenter degree, the error bar is very long compared to others, about 0.15. This is because at most epicenter distance, there is abundant seismic data to stack and make the data, while at 138 epicenter distance, there is little seismic data to work with, therefore the error bar is about 6 times of the normal error bars.

The error bars associated with each epicenter distance are applied in the calculation of CHI^2 mineral physics modelling. The following equation is used:

$$\chi^2 = \sum_{degree}^{range} (IC(Xu'smodel) - IC(Observables))^2 / Error(Observables)^2$$ (Equation 12).More discussion about CHI^2 and amplitude error bars are in next section.

b) Attenuation

Attenuation is the gradual loss of flux as seismic wave travels through material. In [Shearer, 1999], it discusses the methods to deal with it. And in general, this project uses t* method; t* is an integral of dt/Q (quality constant) over the path; amplitude is then multiplied with the variable t*. In particular, this project uses PREM [Dziewonski and Anderson, 1980] model to calculate for t* and Q, and the mantle is divided into 4 segments with different Q values: 3 km to 80km (Q = 600, very high), 80 to 220 (Q = 80), 220 to 670 (Q = 143) and the rest of the mantle (Q = 312). To notice, 0-3 km is left out because of the existence of water, this is because this project studies S waves.

For SS wave, it travels extra path compared to SS precursor. SS wave travels towards the surface of the Earth while SS precursor bounces back from the discontinuity. Therefore, amplitude of SS wave is more attenuated than that of SS precursor wave. This will lead to the overestimate of amplitude ratio, i.e., impedance contrast than the actual impedance contrast from the observables. The more detailed discussion of attenuation about its effect on amplitudes and mineral physics modelling is discussed in the next section. The method of correction is also discussed there.

c) Geometric spreading

As S wave propagates forward, the area that the wave covers become larger but the energy of the wave remains the same, so the intensity of the wave and therefore the amplitude decreases. To account for that, following equation is used [Shearer, 1999].

$$\widetilde{E(\Delta))} = P_{sh}/(4\pi u_1^2 r_1^2 r_2^2 sin\Delta cos\theta 1 cos\theta 2) * ABS(dP_{sh}/d\Delta)) * E_s \text{(Equation 13.)}$$

Because SS wave will travel more path, geometric spreading will affect more on the amplitude of SS wave than it does on SS precursor. Therefore, the same logic as used in attenuation applies, impedance contrast calculated for the observables are greater than the actual value. The more detailed discussion of geometric spreading about its effect on amplitudes and mineral physics modelling is discussed in the next section. The method of correction is also discussed there.

VII. DISCUSSION OF RESULTS

1. 410-km discontinuity

Shown in figure 15 and figure 16, the models for 410-km discontinuity are similar. SUB and global average share similar temperature and basalt fraction values, while MOR is partially global average, from 1500 K to 2500 K with similar basalt fraction. The confidence interval for temperature is from 1000 K - 2500 K, and for basalt fraction is 0.1 – 0.4. The basalt fraction is also more concentrated on the interval of 0.2 - 0.4 basalt fraction.

From geochemistry model shown in figure 16, the upper mantle has a basalt fraction in the vicinity of 16%, while from mineral physics modelling the basalt fraction is known to be within the interval of 20% and 40%. To reconcile such discrepancy of basalt fraction between mineral physics modeling and geochemistry modeling, following corrections are analyzed:

a) Attenuation

The impedance calculated for observables come from the amplitude ratio between S410S and SS. Figure 5 shows the difference in ray paths between the precursor waves and SS waves. The major difference exists when reflection happens at 410-km depth and 660-km depth, while the SS wave travels up to the surface of the Earth. The attenuation structure of the PREM model has a quality factor Q = 600 from 3 km to 80 km, Q = 80 from 80 km to 220 km, and Q = 143 from 220 km to 670 km. When amplitude is calculated, it is divided by the Q factor within the integral. Because 1/Q is very high for the extra travel path for the SS wave, it means S410S is much less attenuated than the SS wave. As amplitude of S410S increases compared to that of SS, the impedance contrast calculated from observations becomes higher than the actual value. Therefore, it is possible that our observations are overestimates of actual impedance contrasts.

This has implications for inferences of composition and temperature. Figure 3 shows that impedance contrast goes down as basalt fraction increases at a fixed temperature. Figure 6 shows as basalt fraction goes up, the impedance contrast at the 410-km discontinuity decreases and disappears completely at high basalt fraction. Therefore, to account for the overestimate of the calculation of impedance contrast, basalt fraction should be pushed towards the right of the chart, which is further away from 16% and towards 100% in Figure 16. In conclusion, the correction doesn't reconcile the discrepancy, instead it would only make the discrepancy worse.

To calculate the actual value of this attenuation-related adjustment, the amplitude should be recalculated using integral equation exp(-w*INTA*(path)/2Q) dt along the path.

b) Geometric Spreading

As discussed in the error section, geometric spreading happens along the path. Because SS wave travels extra path, it means geometric spreading effect happens more to SS wave than to S410S and S660S. The same logic as used in the attenuation discussion applies, impedance contrast calculated for the observables will be more than the actual value. To account for that, once again, the basalt fraction should be pushed further towards right end of the chart. Therefore, the geometric spreading correction doesn't reconcile the discrepancy, instead only making the discrepancy larger.

c) Stack-Defocusing

As discussed in the method section, this project uses stacking method to gather information for heterogeneity. Multiple seismic waves with the same epicenter distance are stacked together. They can start from different locations on the Earth and end in totally different locations, as long as the epicenter distances are the same, they are used in the same stack. As a consequence, the stacked amplitudes of the precursor waves are not always be perfectly aligned, because the amplitudes come in at different times. On the other hand, the SS wave is not be affected. At the time chosen for gathering amplitudes in the stack, many of the samples are not at their maximum. This will result in an underestimate of the actual amplitudes. To account for that in the composition-temperature chart, basalt fraction will be pushed towards left, where 16% is.
The method to fix the problem is to simulate the effects of the stacking method and quantify the error in Matlab: To simulate the defocusing process, multiple normal distribution waves with the same amplitude should be made. Then the waves can be stacked together with some random lag in time to defocus the amplitude. The mean value of the amplitude can be recorded and compared to the maximum amplitude to quantify the effect of defocusing. Then, the actual amplitude of seismic wave can be restored using value quantified from the defocusing simulation.

The discussion presented here does not imply that either geochemistry model is proper nor that the geophysics model is preferred. On the chart of composition and temperature, the geochemistry model is at 16%, and geophysics model is at 20%-40%, which represents larger basalt fractions than the geochemistry model. The first and second corrections push geophysics model towards right, even further away from the geochemistry one, while the third correction can pull back the geophysics model to make it more similar to the geochemistry one.

2. 660-km discontinuity

Figure 16 shows that global average has two regions within the 95% confidence interval. From 1100 K to 1300 K and from 0 to 0.05 basalt fraction, there are three points within the confidence interval. From 1500 K to 1600 K, there is also a long streak of points extending in the basalt fraction axis from 0 to 0.4 basalt fraction. For MOR, there are 3 scattered shapes. The first one is the same as the global average. The second is the global average pattern plus some points at higher temperature at 1700 K to 1900 K. And there is a single point at 2500 K 0.15 basalt

fraction. For SUB, the pattern is similar to MOR. SUB has three areas. The low temperature and 1500 K to 1600 K which are the same as global average, and a single point at 2500 K 0.15 basalt fraction. The patterns for global average, MOR, and SUB are very similar. And the results is similar to the geochemistry model as well, because the basalt fraction at mid-temperature zone is concentrated at 0.15-0.2 basalt fraction. The corrections discussed above for 410-km discontinuity should be made to 660-km discontinuity as well to improve the data accuracy.

VIII. CONCLUSION AND SUGGESTIONS FOR FUTURE WORK

The project proses two hypotheses. The first hypothesis is: An increase in basalt fraction within the mantle transition zone beneath subduction zones will lower the impedance contrast at 410- and 660- km discontinuities compared to the global average. Null: The mantle transition zone discontinuities beneath subduction zones have an impedance contrast no different from the global average. The second hypothesis is: Because oceanic ridges are expected to be shallow (<100 km) features, the impedance contrast of the mantle transition zone discontinuities under mid ocean ridges is similar to the global average.

The project uses mineral physics modeling from Xu's database of the Earth density/velocity profile to estimate the composition and temperature of the upper mantle transition zone. Without corrections discussed above, mineral physics model skew towards a more basalt-rich mantle transition zone compared to the geochemistry model. To restore the alignment of geochemistry and mineral physics model, defocusing should reduce by approximately 50% or more.

For the current estimate, extreme condition of large basalt fractions and high temperature should be ruled out by rule of thumb. Given this condition, for 410-km discontinuity, the global average composition and temperature condition are the stack of mid ocean ridge structure (MOR) and subduction zone structure (SUB): from 1300 K to 2000 K, composition from 20% to 35% basalt fraction. For 660-km discontinuity, the global average is similar to SUB. In addition to the global average condition, MOR has wider range of temperature condition from 1500 K to 1900 K, and composition from 15% to 40% basalt fraction.

The first suggestion to future work is to make the corrections discussed above: attenuation, geometric spreading and stack-defocusing. Therefore more accurate impedance contrast of the observables will be used for the mineral physics modeling. More accurate composition and temperature condition can be inferred for the upper mantle transition zone.

Secondly, the new models can be used in Xu's model to identify the depth of the discontinuities to get better understanding of the transition zone.

IX. ACKNOWLEDGEMENT

I thank my advisor Nicholas C. Schmerr for his instruction on the entire project. This paper would not be finished without his help. I would also like to thank my secondary advisor Quancheng Huang for his support on the data collection and instructions.

I thank my senior thesis professor Philip M. Piccoli for his instruction and efforts on this paper.

I would also like to show my gratitude to the Vedran Lekic for sharing wisdom and opinions with me during the course of this research, although any errors are my own and should not

tarnish the reputations of this esteemed person.

X. BIBLIOGRAPHY:

Ballmer, M.D., Schmerr, N.C., Nakagawa, T., and Ritsema, J., 2015, Compositional mantle layering revealed by slab stagnation at 1000-km depth: Science Advances, 1, 11.

Bassin, C.G.L., Laske, G., and Masters, G., 2000, The current limits of resolution for surface wave tomography in North America. EOS Trans AGU 81:F897.

Chambers, K., Deuss, A., and Woodhouse, J.H., 2005, Reflectivity of the 410-km discontinuity from PP and SS precursors: Journal of Geophysical Research: Solid Earth, 110.

Crotwell, H.P., Owens, T.J., and Ritsema, J., 1999, The TauP Toolkit: Flexible Seismic Travel-time and Ray-path Utilities: Seismological Research Letters, 70, 154-160.

DeMets, C., Gordon, R. G., Argus, D. F., and Stein, S., 1989, Current plate motions: Geophysical Journal International, 101, 425-478.

Dziewonski, A.M., and Anderson, D.L., 1980 preliminary reference earth model: Physics of the Earth and Planetary Interiors, 25, 1038.

Flanagan, M.P., and Shearer, P.M., 1999, A map of topography on the 410-km discontinuity from PP precursors: Geophysical Research Letters, 26, 549-552.

Hayes, G. P., Wald, D. J., and Johnson R. L. 2012, Slab1.0: A three-dimensional model of global subduction zone geometries, Journal of Geophysical Research: Solid Earth, 117, B01302.

Ringwood, A.E., 1982, Phase Transformations and Differentiation in Subducted Lithosphere: Implications for Mantle Dynamics, Basalt Petrogenesis, and Crustal Evolution: The Journal of Geology, 90, 611-643.

Ringwood, A. E., 1975, Composition and Petrology of the Earth's Interior, 618.

Sandvol, E., and Hearn, T. 1994. Bootstrapping Shear-Wave Splitting Errors, Bulletin of the Seismological Society of Amekica, 84, 1971-1977.

Schmerr, N., and Garnero, E., 2006, Investigation of upper mantle discontinuity structure beneath the central Pacific using SS precursors: Journal of Geophysical Research, 111.

Shearer, P. M., 1999. Introduction to seismology. Cambridge: Cambridge University Press, 303.

Xu, W., Lithgow-Bertelloni, C., Stixrude, L., and Ritsema, J., 2008, The effect of bulk composition and temperature on mantle seismic structure: Earth and Planetary Science Letters, 275, 70-79.